

---

## **Application of Vibration-based Damage Detection Algorithms to Experimental Data from Multi-story Steel Structures**

---

**Yizheng Liao, Konstantinos Balafas, Anne S. Kiremidjian, Ram Rajagopal**

Department of Civil & Environmental Engineering,  
Stanford University, Stanford, CA, USA  
E-mail: yzliao@stanford.edu, konstantinos.balafas@gmail.com,  
ask@stanford.edu, ramr@stanford.edu

**Chin-Hsiung Loh**

Department of Civil Engineering,  
National Taiwan University  
E-mail: lohc0220@ntu.edu.tw

**Abstract:** Recently, vibration-based statistical pattern recognition (SPR) has received significant attention in the field of structural health monitoring (SHM). There has been remarkable progress in the development of data acquisition systems and statistical damage detection algorithms. However, many of them have not been validated or calibrated by experimental data. This paper presents and analyzes a recent shake table experiment of two three-story steel frame structures. In this experiment, the structural damage was introduced in a systematic and controlled way and the structures were tested with different levels of earthquakes. Three types of analyses were conducted. First, SnowFort, a wireless sensor system designed for infrastructure monitoring, was deployed and vibration measurements obtained from the system were compared to conventional wired sensors. It is shown that the wireless sensors used within the SnowFort system achieve the same accuracy as the wired sensors. Second, the Rotation Algorithm is applied to the obtained data to estimate residual displacements in the structures. Excellent agreement is found between the estimates and the residual displacements obtained from direct measurements using the linear variable differential transducers. And third, a Continuous Wavelet Transform-based damage detection algorithm is applied to the experimental data. The results show that the distributions of wavelet model parameters are sensitive to the state of damage and loading conditions and thus can be used for damage diagnosis.

**Keywords:** Structural Health Monitoring, Wireless Sensor Network, Damage Detection, Experimental Study, Statistical Pattern Recognition

---

## 1 Introduction

Recent global seismic disasters, such as those in Chile, China, Japan, and Nepal, have caused significant damages in or near urban areas. Some structural damage caused by an earthquake can be immediately observed, such as collapse or partial collapse. However, many types of damage are hidden within a structure, such as those encased in concrete [1] or are behind sheet rock. These types of damage, which are difficult, expensive in some cases impossible to investigate visually, can still pose a risk to the overall health of the structure and to its occupants.

During the past several decades, Structural Health Monitoring (SHM) systems have been shown to provide quick evaluation of structural damage after earthquakes and other extreme events. Ideally, a SHM system should detect and locate damage and should assess its severity. Statistical pattern recognition (SPR) methods are receiving significant attention, especially in the context of vibration analysis of structures. The statistical pattern recognition paradigm for SHM can be summarized in four steps [2, 3, 4]: 1) operational evaluation; 2) data acquisition; 3) feature selection and information condensation; and 4) statistical model development for feature discrimination. Recently, several emerging data acquisition systems and damage diagnosis methods are proposed. For example, with the development of sensing technology, wireless sensor networks have shown promise to be deployed in large-scale for health monitoring [5, 6, 7, 8]. The wireless sensors overcome several disadvantage of wired and analog sensors, such as difficult to install, high cost of maintenance, and limited mobility. For structural damage detection, there have been significant efforts in the applications of various SPR methods [9, 10, 11, 12, 13, 14]. Several comprehensive surveys are given by [15, 4]. In SPR, damage is detected through changes or outliers in statistical features rather than changes of the structural properties. These statistical features are directly extracted from the acquired data. As a result, SPR-based damage detectors do not require any knowledge about the structural properties. This allows us to perform the analysis at the sensor locations as well as to combine features from multiple locations for a more comprehensive structural health assessment.

Although there have been numerous research studies on the application of wireless sensor networks in SHM and statistical damage detection algorithms, unfortunately, many of them have not been validated and calibrated by laboratory experiments whereby damage is introduced in a systematic and controlled way. In this paper, we introduce a recent shake table test conducted at the National Center for Research on Earthquake Engineering (NCREE) in Taipei, Taiwan. This experiment has three objectives: (1) validate the system performance and accuracy of SnowFort, a new open source wireless infrastructural monitoring system [16]; (2) evaluate a residual displacement estimation algorithm referred to as the Rotation Algorithm [17]; (3) test an acceleration-based structural damage detection algorithm based on the Continuous Wavelet Transform [18] via experimental data. To satisfy these objectives, two identical structures were constructed and were tested with different levels of ground motions introducing gradually increasing damage. In addition, different types of wireless and wired sensors, including three dimensional accelerometers and gyroscopes, strain gauges and linear variable differential transducers, were installed to collect measurements, which were used to validate the wireless monitoring system and the damage detection algorithms. It should be noted that accelerometers and gyroscopes were used with the wireless system, while the conventional wired system collected data from accelerometers, strain gauges and linear variable differential transducers.

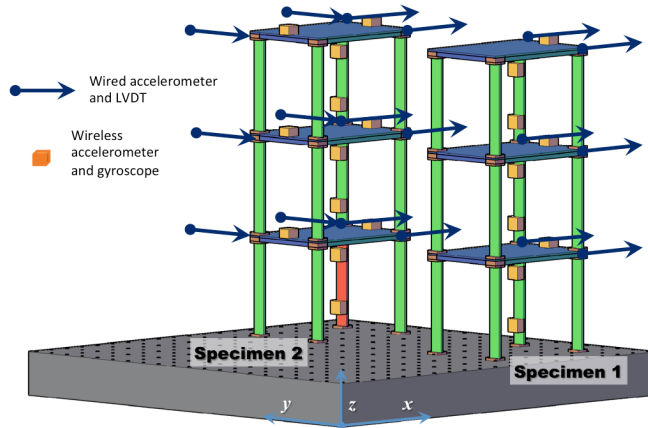


**Figure 1:** Two structures and sensor locations used at the NCREE experiment. The weakened column is in red.

In this paper we will first describe the experiment with details on the specimens and the sensors. Then the performances of SnowFort will be analyzed on packet drop rate, power consumption, and the measurement accuracy. Next, we evaluate the Rotation Algorithm to estimate residual displacement. Furthermore, the Continuous Wavelet Transform-based algorithm will be demonstrated to be sensitive to the physically identified and observed damage states thus demonstrating that statistics of wavelet coefficients can be used to detect structural damages. The conclusions from the study will be presented at last.

## 2 Experiment Design and Data Acquisition Systems

### 2.1 Description of Experiment

This experiment was designed and performed at NCREE. Two identical three story single bay steel frames were constructed specifically for this experiment. Both structures have an inter story height of 1.1m. The floor dimensions at every story are 1.1m × 1.5m. The columns have rectangular cross-sections with a dimension of 0.15m × 0.025m × 1.06m. As indicated in Fig. 1, for Specimen 2, the NW column is replaced with a weakened column, which has a thickness of 0.015m. Thus, Specimen 1 is a symmetric structure while Specimen 2 is non-symmetric. Fig. 2 shows these two structures in the experimental facility.

These two structures were placed side by side on the same shake table. The record of the 1999 Chi-Chi earthquake Station TCU 071 was used as the base excitation of the experiment. The excitation was applied in the x-direction with amplitudes progressively increasing from 100 to 1450 gals. Fig. 3 shows an example of the earthquake signal with a peak of 1000 gals. White noise excitations with 50 gals peak amplitude were applied between strong motion runs. Total 25 runs were conducted during the experiment. The earthquake amplitudes are summarized in Table. 1 and correspond to the peaks of the vibrations to which the shake table was subjected. For the first 10 runs, a 500 kg mass block was placed on every story of both specimens to simulate the weight of a real structure. For Run 11 and Run 12, an additional 500 kg mass block was added on the roof of each specimen.



**Figure 2:** Photo of two structures (in green) on the shake table. The front one is Specimen 1 and the back one is Specimen 2.

**Table 1** Summary of Ground Motions

Run Number	Desired Amplitude (gal)	Achieved Amplitude (gal)
1	100	95
2	250	269
3	400	400
4	550	572
5	700	674
6	850	858
7	1000	994
8	1150	1190
9	1300	1329
10	1450	1329
11	850	850
12	1000	1000

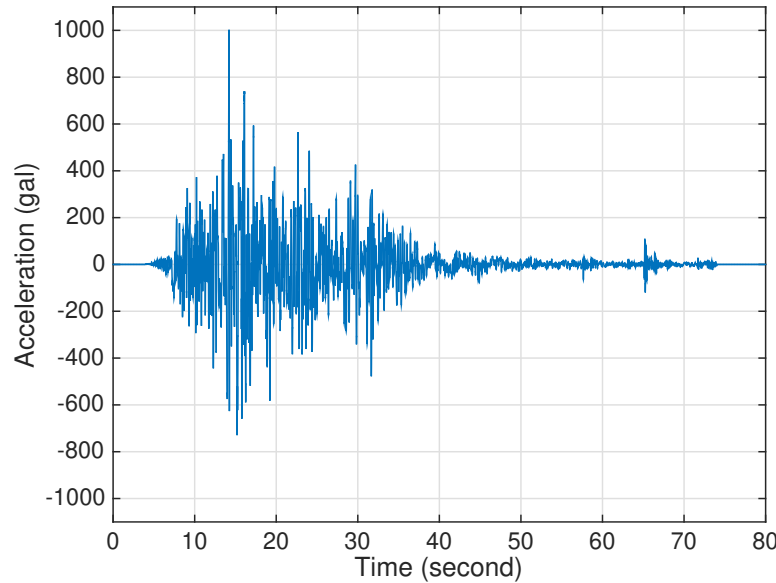


**Figure 3:** Earthquake signal of 1999 Chi-Chi earthquake. The signal was collected at Station TCU 071 and was scaled to have a peak of 1000 gal.

## 2.2 Data Acquisition Systems

In this experiment, both wired and wireless sensors were installed for data acquisition. The summary of sensors is given in Table 2. All the analog sensors were connected with a common Analog-to-Digital Converter (ADC) with a sampling frequency of 200Hz. The cut-off frequency of the anti-aliasing filter was 50Hz. Each wireless sensing device was assembled with a Telosb mote [19, 20] and a 16-bit digital sensor, including a three-axis accelerometer and a three-axis gyroscope [21], as shown in Fig. 4. These motes were operating within the SnowFort system, an open source wireless sensor system designed for infrastructure monitoring [16, 22]. The motes and sensors were powered by two standard AA batteries. The data were collected at 51.2Hz sampling frequency and filtered with a 20Hz anti-aliasing filter. The sampling frequency is fractional because the on-board microprocessor used 1024 ticks to represent one second and we set the mote to sample every 20 ticks. For the first 9 runs, the wireless accelerometers had a measurement range of  $\pm 2\text{g}$ . The sensitivity was 16384 least significant bits (LSB) per g. The gyroscopes had a range of  $\pm 250$  degrees per second ( $^{\circ}/\text{sec}$ ) with a sensitivity of 131 LSB per  $^{\circ}/\text{sec}$ . For the last three runs, the ranges of both accelerometer and gyroscope were increased. The range of the accelerometer was increased to  $\pm 8\text{g}$  with a sensitivity of 4096 LSB/g. The range of gyroscope was  $\pm 1000^{\circ}/\text{sec}$  with a sensitivity of 32.8 LSB per  $^{\circ}/\text{sec}$ . According to [21], the accelerometer has an average noise level of 1.265 mg and the gyroscope has an average noise level of 0.016 $^{\circ}/\text{sec}$ .

The sensor installation locations are shown in Fig. 1. The wired accelerometers and linear variable differential transducers (LVDTs) were installed on each floor. For Specimen 1, accelerometers and LVDTs only measured the vibration along x-axis, which was also the shaking direction. For Specimen 2, since one column was replaced with a weakened one, the vibrations along both x-axis and y-axis were recorded. The wireless sensors were

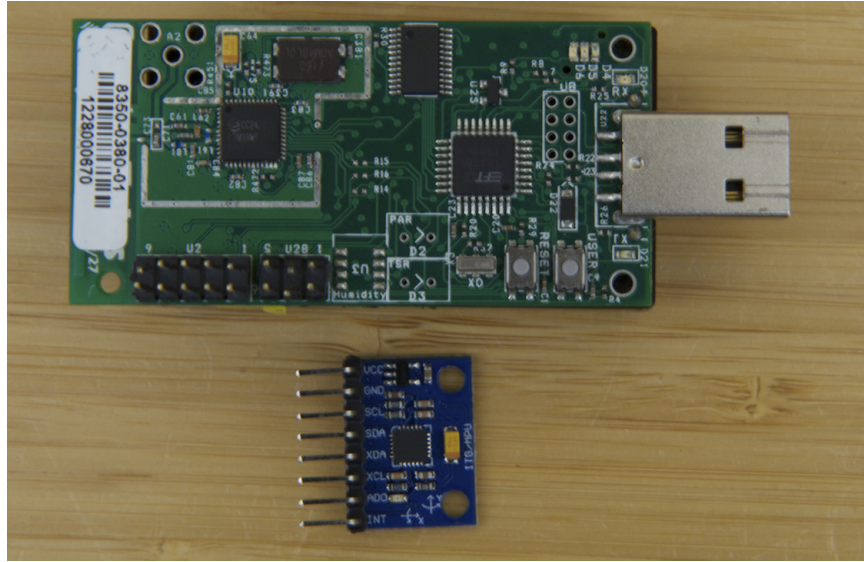


**Figure 4:** The green device (upper) is the TelosB mote with TI MSP430 microprocessor and CC2420 Zigbee transceiver. The blue device (lower) is the MPU 6050 digital sensor with one three-axis accelerometer and one three-axis gyroscope.

**Table 2** Summary of Sensors

Sensor Name	Sensor Type	Model	Total
1-D accelerometer	analog & wired	Setra 141B MTS	18
LVDT	analog & wired	Tempsonics G	19
Strain gauge	analog & wired	Tokyo Sokki Kenkyuj	27
Thin film	analog & wired	—	12
Optical sensor	optical & wired	Optotrak Certus	28
3-D accelerometer & gyroscope	digital & wireless	MPU6050	21

placed on the floors and the columns, as shown in Fig. 1. The sensors on the columns were about 0.28m and 0.83m above each floor level in order to avoid potential region of column hinge formation. The wireless sensors, which were installed on the floors, were located at the midpoints of opposite edges of each floor. Since all wireless sensors were three-axis, the vibrations along all directions were collected.

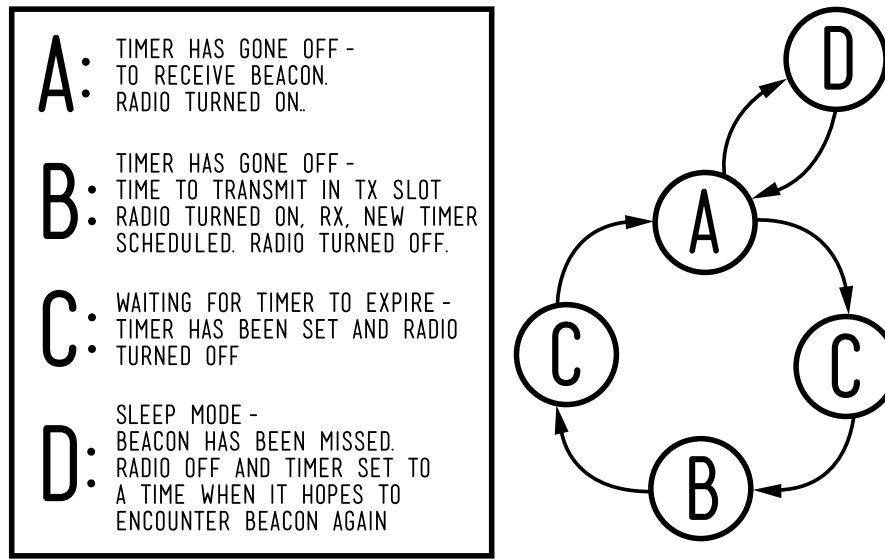


Figure 5: State machine of SnowFort TDMA protocol [16].

In this experiment, each wireless sensing unit was equipped with a Zigbee radio and sent sampled data to a base station, which was a Raspberry Pi [23], a single-board Linux computer with Wi-Fi connection. The sensing units implemented a customized Time Division Multiple Access (TDMA) protocol as the medium access control (MAC) layer. In this TDMA protocol, each sensing unit was assigned a unique transmission window and transmitted sampled data to the base station periodically. When the mote was not permitted to transmit, it turned off its radio for power saving. A summary of the SnowFort TDMA protocol is shown in Fig. 5. Compared with other well-known MAC protocols, such as Carrier Sense Multiple Access (CSMA), which is used in several Wi-Fi standards, TDMA is simple, collision free, and power efficient. In this test, each mote was assigned a 31.25 ms time slot. To synchronize the motes, all motes used the beacon message received from the base station to adjust their local clocks. Four base stations were deployed to ensure the high quality of signal reception and were placed at different locations in the experiment facility. Each mote was assigned to communicate with only one base station. To avoid the collision among the motes associated with different base stations, we assigned a unique frequency channel within 2.4GHz public band to each base station and the associated motes. This technique is also known as Frequency Division Multiple Access (FDMA). The base stations were synchronized by the network time protocol (NTP).

### 2.3 SnowFort System Evaluation

In this section, we will evaluate the performance of SnowFort system from three aspects: network reliability, quality of sensor measurements, and power consumption.

#### 2.3.1 Network Reliability

For evaluating the reliability of SnowFort, we analyze the Packet Drop Rate (PDR), which is defined as follows:

$$\text{PDR} = \left( 1 - \frac{\text{Number of packet received}}{\text{Number of packet expected}} \right) \times 100\%. \quad (1)$$

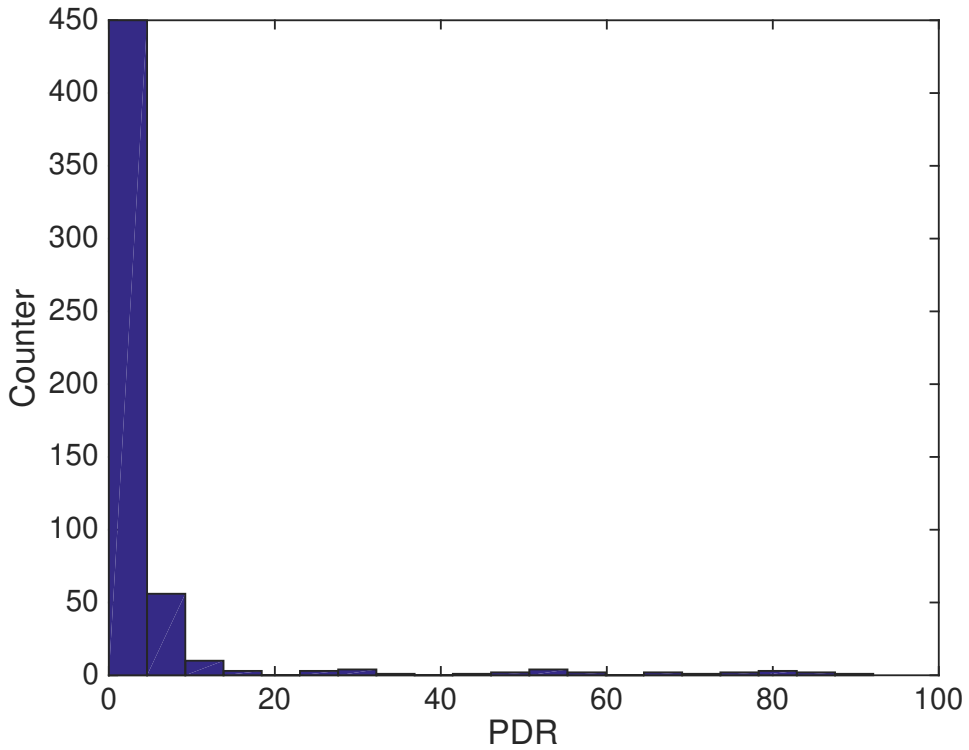


**Figure 6:** The histogram of PDR of all testings and motes.

The PDRs of each experiment and each sensor are summarized in Fig. 6. The overall PDR is 5.746%. This result is better than the performance of the system presented in [24], which needs to retransmit more than 9.5% of total packets. As described in the previous section, SnowFort uses TDMA protocol, which is a single-hop scheme. In [24], the single-hop communication scheme has similar performance as SnowFort but the multiple-hop protocol is worse. This shows the reliability of the TDMA protocol.

Fig. 7 shows the box plots of PDR of each mote. Besides Mote 12, all the motes have an average PDR below 5%. Mote 12, which was installed on the roof of Specimen 2, had

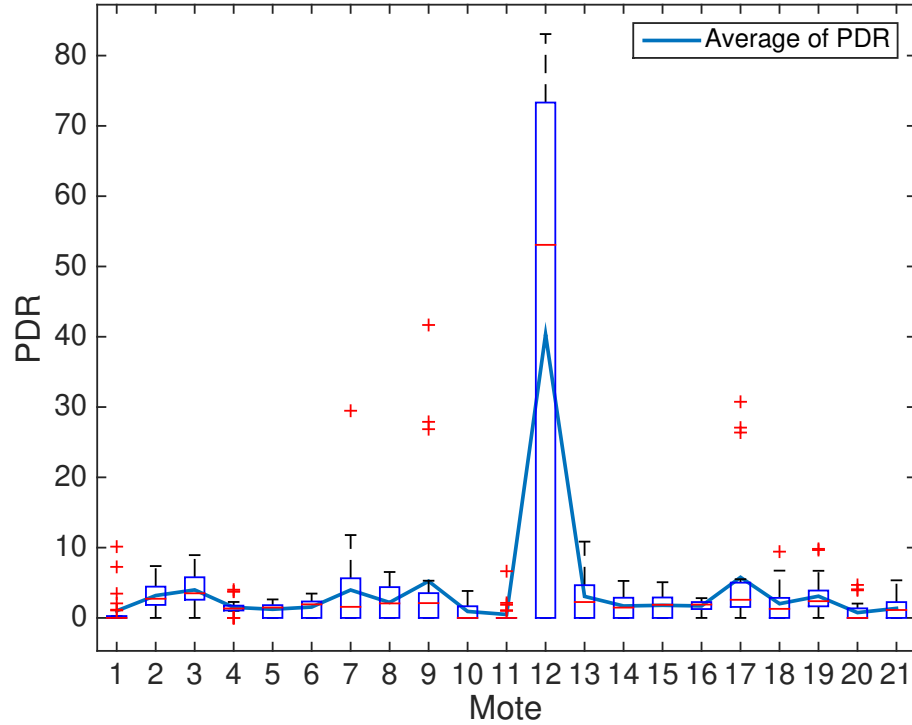


**Figure 7:** The box plot of PDR of motes.

the largest PDR because the communication channels were blocked by a material mass block in the experiment. In [25], the deployed system has an average PDR of 1.25%. In our experiment, more than half of the motes have equivalent or better performance. In [25], the average received signal strength indicator (RSSI) value of the packets received at the base station is -48.3 dBm, which is higher than many of our motes. The average RSSI value of our motes is about -75 dBm in this experiment. With a more powerful antenna or the enable of retransmission, SnowFort can achieve an equivalent or better performance.

### 2.3.2 Quality of Sensor Measurements

Fig. 8 and Fig. 9 show the measurements of wired and wireless accelerometers in Run 4. The sensors and runs are chosen randomly. We can observe that both sensors have identical measurements. To numerically compare the difference, we compute the root mean squared error (RMSE). The measurements collected by wired accelerometers are downsampled to the sampling frequency of 51.2Hz, which is as same as the sampling frequency of the wireless sensors. Then, we compute the RMSE between the samples of wired and wireless sensors. The RMSE between the wireless and wired measurements is 0.002g.

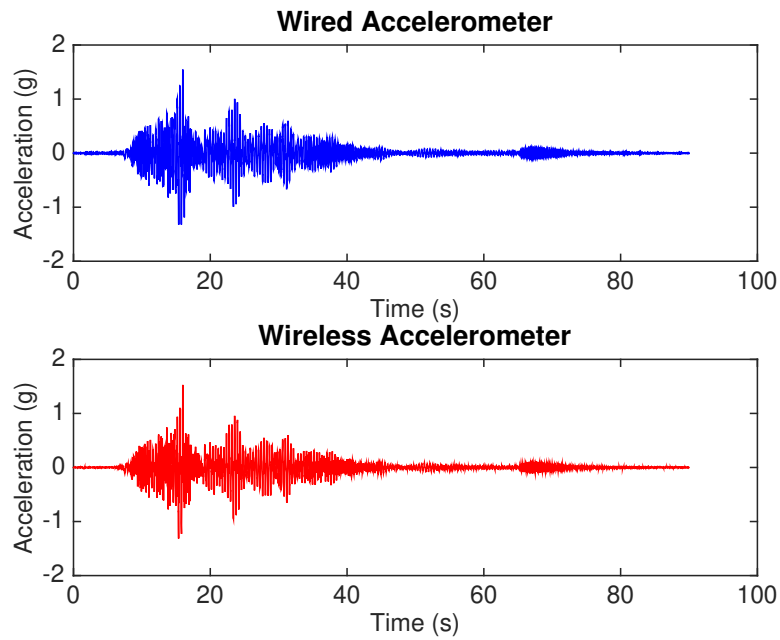


**Figure 8:** Measurements of wired and wireless accelerometers in Run 4.

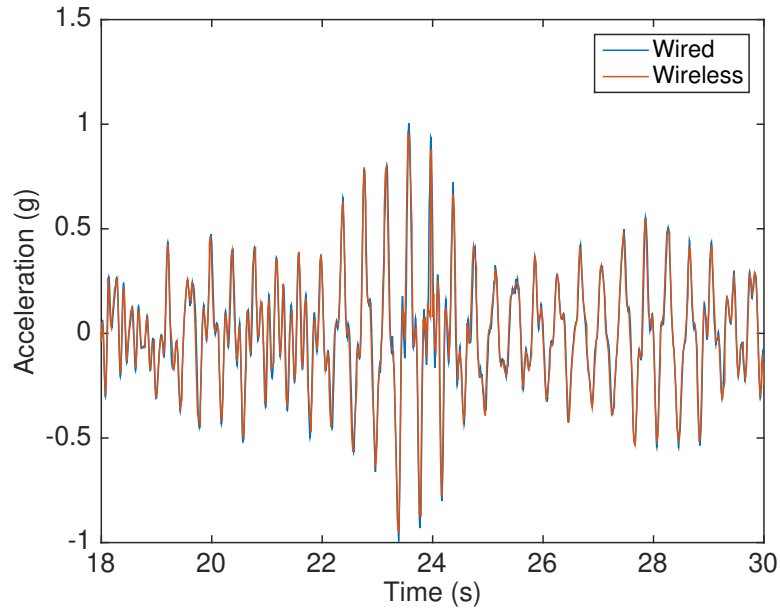


**Figure 9:** Close up comparison of wired and wireless accelerometers.

### 2.3.3 Power Consumption

In this test, all motes were powered by standard AA batteries. With the integration of both gyroscope and accelerometer, the estimated lifetime of one mote is about 28 days [16]. During the 4-days testing, all motes were operating 24 hours. The base stations were only turned on during daytime. During the non-experiment time, the base stations were off and the TDMA protocol turned the radios into the Sleep Mode. Meanwhile, the digital sensors were still functioning. Over the 4-days testing, only three out of 21 sensors had a battery replacement because the voltages of these batteries drifted below the operational voltage of mote.

In summary, we have validated that the recently developed wireless sensor network system, SnowFort, is robust and power efficient for vibration-based structural health monitoring. In addition, the RMSE results show that the wireless sensors have the same accuracy as the analog sensors. Compared with the wired sensors, the wireless sensors have many advantages, such as small size, low power consumption, and the ease of installation and maintenance. This proof-of-concept experiment results will allow us to use wireless sensing units alone for SHM in the future.

## 3 Estimation of Residual Displacement Using Rotation Algorithm

The residual displacement of the structure after an earthquake is a simple yet reliable indicator of potential damage. Direct displacement measurements in the laboratory can be performed with LVDT. On a real structure, displacement measurements are typically obtained by laser interferometers. During an earthquake, it is impossible to obtain direct displacement measurements with laser interferometer, because the sensor will displace at a different rate than the structure. Another approach to estimating floor displacement on a structure subjected to earthquake motion is to double integrate acceleration measurements. This approach leads to a very large error in displacement estimates. In [26], the authors proposed an algorithm that utilizes Micro-Electro-Mechanical System (MEMS) accelerometers to estimate the residual displacement of bridge columns.

The proposed algorithm is developed on the premise that ambient vibrations are measured before and immediately after an earthquake. These measurements are then used to compute the rotation of the column at the location of the sensor. It is assumed that the plastic rotation in a bridge column is concentrated at a plastic hinge location at the base of the column and the rest remains elastic. The residual displacement of the column is estimated by calculating the length of the plastic hinge region based on [27] and assuming that all of the rotations are concentrated at mid-height of the hinge.

Some recent studies, such as [28], have shown that the estimator in [27] may underestimate the true plastic hinge length, which leads to the overestimate of the residual displacement obtained from the algorithm in [26]. For this reason, in [17], the authors extend the rotation algorithm to use the recordings of multiple sensors. Multiple sensors along the height of the structure are selected and the rotations at the sensor locations are computed before and immediately after an earthquake based on the ambient vibration measurements. Let  $a_x$  and  $a_z$  denote the acceleration measurements along the shaking direction and along

the gravity direction respectively. If the structure is symmetric, the rotation  $\theta$  is estimated as follows:

$$\hat{\theta} = \arctan\left(\frac{a_x^{\text{after}}}{a_z^{\text{after}}}\right) - \arctan\left(\frac{a_x^{\text{before}}}{a_z^{\text{before}}}\right), \quad (2)$$

where  $a_x^{\text{before}}$  refers to the acceleration before earthquake and  $a_x^{\text{after}}$  refers to the acceleration after earthquake. The measurement noise of acceleration affects the estimation accuracy of  $\hat{\theta}$ . To minimize the impact of measurement noise, we use the average of samples before and after earthquakes to estimate  $\hat{\theta}$  in Equation (2), e.g.,  $a_x^{\text{before}} = (\sum_{n=1}^N a_x^{\text{before}}[n])/N$ .

After estimating  $\hat{\theta}$ , the rotations estimated at each sensor location are fitted with a polynomial function. For example, if the rotation estimates are fitted with a forth order polynomial function, we have

$$\hat{\theta} = \beta_1 H^4 + \beta_2 H^3 + \beta_3 H^2 + \beta_4 H + \beta_5, \quad (3)$$

where  $H$  denotes the height of the sensor above ground. Although many sensors have equipped both accelerometers and gyroscopes, we cannot directly use gyroscopes to estimate the permanent rotations because gyroscopes measure the angular velocity and have nearly zero readings during steady state or ambient vibration.

After that, the fitted polynomial function is integrated with respect to the structural height to provide a function that estimates the residual displacement  $D$ , as shown below:

$$\begin{aligned} \hat{D} &= \int (\hat{\beta}_1 H^4 + \hat{\beta}_2 H^3 + \hat{\beta}_3 H^2 + \hat{\beta}_4 H + \hat{\beta}_5) dH \\ &= \frac{\hat{\beta}_1}{5} H^5 + \frac{\hat{\beta}_2}{4} H^4 + \frac{\hat{\beta}_3}{3} H^3 + \frac{\hat{\beta}_4}{2} H^2 + \hat{\beta}_5 H. \end{aligned} \quad (4)$$

Since the structure base is assumed to be fixed, we assume that there is no displacement at the base. Hence, the intercept term is zero and is ignored in (4).

When the structure is non-symmetric, e.g. Specimen 2, torsion and out-of-plane movement are expected. Therefore, we need to deploy the acceleration signals collected in all three directions. Let  $a_y$  denote the acceleration measurements that are perpendicular to both shaking direction and gravity direction. Then, we can compute the rotations of x-axis  $\theta_x$  and y-axis  $\theta_y$  as follows:

$$\begin{aligned} \hat{\theta}_x &= \arctan\left(\frac{a_x^{\text{after}}}{\sqrt{(a_y^{\text{after}})^2 + (a_z^{\text{after}})^2}}\right) \\ &\quad - \arctan\left(\frac{a_x^{\text{before}}}{\sqrt{(a_y^{\text{before}})^2 + (a_z^{\text{before}})^2}}\right), \end{aligned} \quad (5)$$

$$\begin{aligned} \hat{\theta}_y &= \arctan\left(\frac{a_y^{\text{after}}}{\sqrt{(a_x^{\text{after}})^2 + (a_z^{\text{after}})^2}}\right) \\ &\quad - \arctan\left(\frac{a_y^{\text{before}}}{\sqrt{(a_x^{\text{before}})^2 + (a_z^{\text{before}})^2}}\right). \end{aligned} \quad (6)$$

Then, we can apply Equations (3) and (4) to estimate the residual displacements of x-axis and y-axis respectively.

The calculation of the rotation measurements can be embedded on the microprocessor of sensing units, thus requiring the transmission of only the final rotation values. While the estimation of displacements requires the rotations from all sensors, the calculations involved can also be embedded on the microprocessor of the base station, which can then report the estimated displacements directly to the end user. The residual displacements can then be correlated to the degree of damage depending on the material, type of structural framing and height of the structure. Thus, the Rotation Algorithm provides a computationally efficient method to obtain reliable information on the residual displacements of a structure almost immediately after an extreme loading event.

### 3.1 Experimental Results

In order to estimate the displacements, the measurements collected by the wireless sensors installed on the columns are selected. As we have discussed previously, the story height is  $H = 1.1\text{m}$ . All sensors in the same specimen are utilized and a fourth order polynomial is used to estimate the residual displacements  $\hat{D}$ . The rotations at the sensor locations are calculated using 500 points (approximately 10 seconds) of ambient vibration before and after each ground motion. For Specimen 1, which is expected to deform in one plane, the two-dimensional version of the algorithm is applied, which is presented by Equation (2).

Fig. 10 shows a comparison between the estimated displacements and direct displacement measurements obtained through LVDTs. The baseline is the displacement at the beginning of each run and the residual displacements are computed at the end of each run. Equation (3) is fitted using the least square method, which minimizes the squared errors. For the full specimen, the mean squared error (MSE) is 0.004. It should be noted that the rotations were measured and computed at the locations of the wireless sensors (two per story). But the displacements reported in Fig. 10, which are estimated by using Equation (4), are at the floor heights, where LVDTs were installed. This highlights the capability of the Rotation Algorithm to estimate the displacement at any point along the height of a structure as well as the accuracy of the wireless sensors. From the figure, we can observe that the maximum gap between the estimate and true displacement is less than 1 mm.

In the case of Specimen 2, where torsion and out-of-plane movement are expected, the three-dimensional version of the algorithm is applied, as shown in (5) and (6). The estimated and measured displacements for the shaking direction are shown in Fig. 11. Run 7 is missing due to an unexpected power outage of the wireless base station during the test. Similar to Specimen 1, the estimates of residual displacements are accurate and very close to the true measurements. In Fig. 11, we also plot the displacement estimates by using the 2-D rotation algorithm. We can observe that the estimates of two- and three- dimensional algorithms are nearly identical. The reason is that the residual displacement in the out of plane direction (y-axis) is very small (maximum residual drift < 0.1%).

In summary, we demonstrate that the recently proposed Rotation Algorithm is accurate and robust for residual displacement estimation. The estimated displacements are close the LVDT measurements. This shows the reliability of Rotation Algorithm and enables to use wireless sensors for stand-alone rotation and displacement estimation.

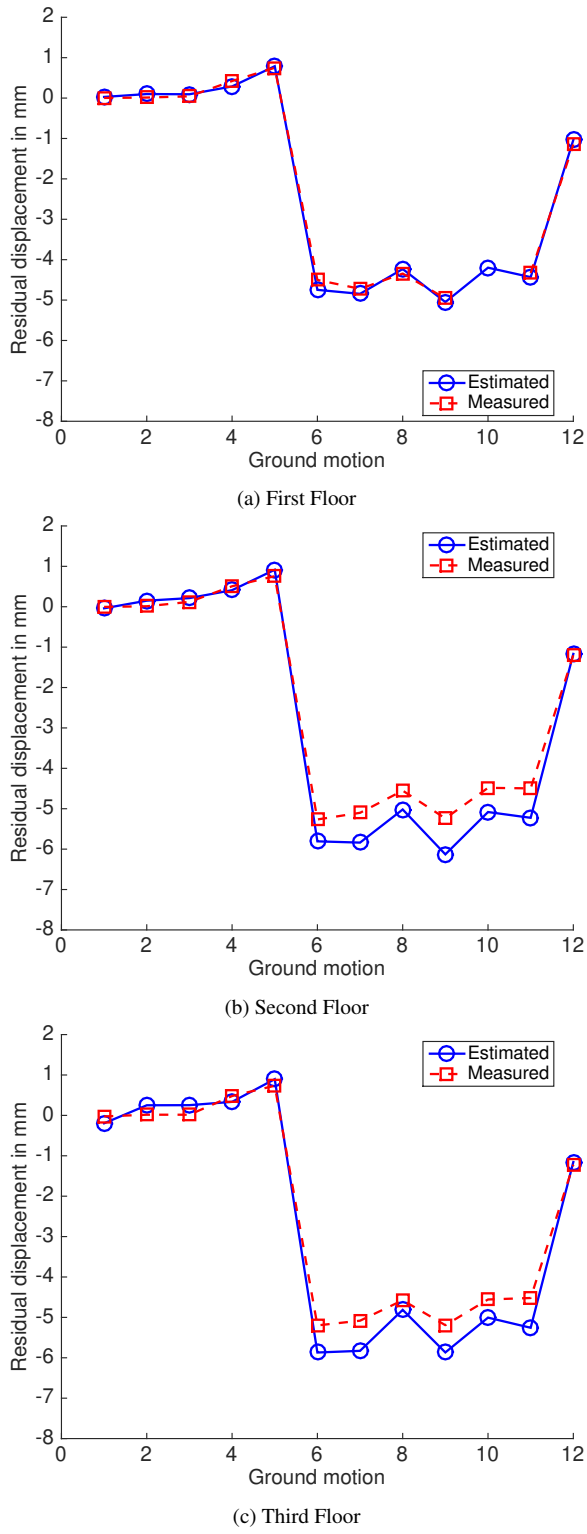


**Figure 10:** Estimated and measured residual displacements for Specimen 1 in the shaking direction (X-axis).

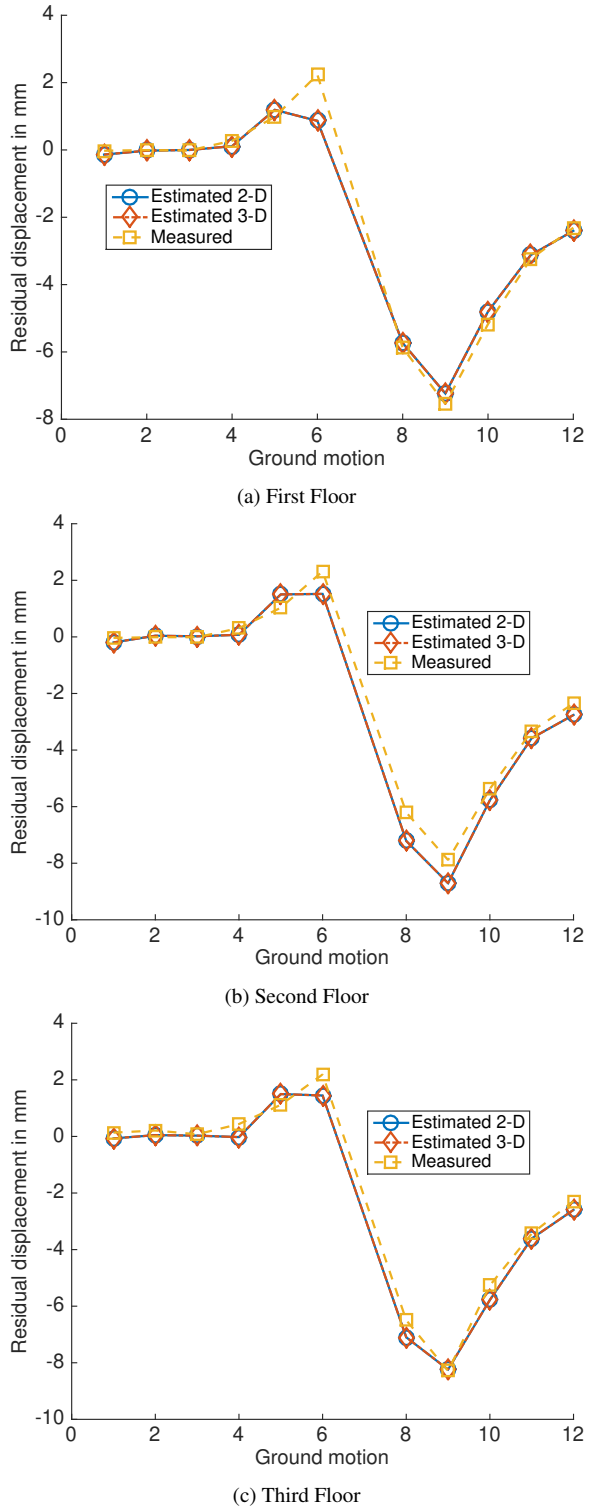


**Figure 11:** Estimated and measured residual displacements for Specimen 2 in the shaking direction (X-axis).

#### 4 Wavelet-based Damage Detection Algorithm

Wavelet-based damage detection algorithms have been widely used in SHM, especially under the Statistical Pattern Recognition paradigm [29, 30, 31]. In a recent paper [18], the authors propose a Continuous Wavelet Transform (CWT)-based damage detection algorithm. In this algorithm, the wavelet coefficients at each time sample is modeled as a Gaussian Process. A damage is declared when the model parameters do not have the same statistics as the undamaged model parameters.

Let  $a(u)$  denote the acceleration response collected at time  $u$ . The Continuous Wavelet Transform of  $a(u)$ ,  $Wa(t, s)$ , is defined as

$$Wa(t, s) = \int_{-\infty}^{\infty} a(u) \frac{1}{\sqrt{s}} \psi^* \left( \frac{u-t}{s} \right) du, \quad (7)$$

where  $t$  denotes the *shift* (a measure of time),  $s$  denotes the *wavelet scale* (a measure of frequency), the function  $\psi$  denotes the wavelet function, and the operator  $(.)^*$  is the complex conjugate. At shift  $t$ , the wavelet coefficient  $y_s(t)$ , which is also referred as the wavelet “slice” at time  $t$ , is

$$\begin{aligned} y_s(t) &= Wa(t, s) \\ &\triangleq a_t \Psi_t(b_t s + c_t) + \Delta y(s), \end{aligned} \quad (8)$$

where  $a_t$  denotes the amplitude parameter,  $b_t$  denotes the stretch parameter, and  $c_t$  denotes the shift parameter. These parameters represent the effect of input motion on the system’s response, such as amplitude and frequency content.  $\Delta y(s)$  is an error term that captures the information not explained by the first term. The function  $\Psi_t(s)$  is a realization of the fundamental shape of the wavelet slices at time  $t$ , i.e.

$$\Psi_t(s) = \bar{\Psi}(s) + \epsilon_t(s), \quad (9)$$

where  $\bar{\Psi}(s)$  is the fundamental shape of the wavelet slices and only depends on the structural damage state and  $\epsilon_t(s)$  is the residual term. Therefore, to declare whether a damage occurs or not, by assuming that  $\bar{\Psi}(s)$  is a random process and represents the wavelet shape of the undamaged state, we can do the following hypothesis testing:

$$\begin{aligned} \mathcal{H}_0 : \quad &\Psi_t(s) = \bar{\Psi}(s) + \epsilon_t(s) \quad (\text{Undamaged}) \\ \mathcal{H}_1 : \quad &\Psi_t(s) \neq \bar{\Psi}(s) + \epsilon_t(s) \quad (\text{Damaged}) \end{aligned}$$

Typically,  $\bar{\Psi}(s)$  is unobservable. Since a wavelet slice is defined by three model parameters, amplitude  $a_t$ , stretch  $b_t$ , and shift  $c_t$ , the change of the model parameters lead to the change in the wavelet shape. Thus, alternatively, we can test if these model parameters follow the same distributions as the parameters of the undamaged wavelet slice. For example, for the amplitude parameter  $a_t$ , the hypothesis testing becomes:

$$\begin{aligned} \mathcal{H}_0 : \quad &a_t = a_0 \quad (\text{Undamaged}) \\ \mathcal{H}_1 : \quad &a_t \neq a_0 \quad (\text{Damaged}) \end{aligned}$$

where  $a_0$  is the amplitude parameter of the undamaged wavelet slice.

To obtain the model parameters of undamaged wavelet slices, we need to select a reference slice. In this paper, the reference slice is selected manually so that it is relatively smooth and its general shape represents the major shape of the rest of the slices. A detailed study on how to select the reference slide is presented in [32]. By combining (8) and (9), the reference slice  $y_0(s)$  can be written as

$$\begin{aligned} y_0(s) &= a_0 \Psi_t(b_0 s + c_0) + \Delta y(s) \\ &= a_0 \bar{\Psi}(b_0 s + c_0) + a_0 \epsilon_t(b_0 s + c_0) + \Delta y(s). \end{aligned}$$

Now, for each newly available wavelet slice  $y_t(s)$ , we obtain:

$$\begin{aligned} y_0(s) &= \frac{a_0}{a_t} y_t \left( \frac{b_0}{b_t} s + \frac{c_0 - c_t}{b_t} \right) \\ &\quad - a_0 \epsilon_t(b_0 s + c_0) - \frac{a_0}{a_t} \Delta y \left( \frac{b_0}{b_t} s + \frac{c_0 - c_t}{b_t} \right) \\ &\quad + a_0 \epsilon_0(b_0 s + c_0) + \Delta y(s). \end{aligned} \quad (10)$$

Defining the following:

$$\tilde{a}_t = \frac{a_0}{a_t} \quad (11a)$$

$$\tilde{b}_t = \frac{b_0}{b_t} \quad (11b)$$

$$\tilde{c}_t = \frac{c_0 - c_t}{b_t} \quad (11c)$$

$$\tilde{\epsilon}_t(s) = a_0 \epsilon_0(b_0 s + c_0) - a_0 \epsilon_t(b_0 s + c_0) \quad (11d)$$

$$\tilde{\Delta}y(s) = \Delta y(s) - \tilde{a}_t \Delta y \left( \tilde{b}_t s + \tilde{c}_t \right), \quad (11e)$$

(10) becomes:

$$y_0(s) = \tilde{a}_t y_t \left( \tilde{b}_t s + \tilde{c}_t \right) + \tilde{\epsilon}_t(s) + \tilde{\Delta}y(s) \quad (12)$$

$$= y'_t(s) + \tilde{\epsilon}_t(s) + \tilde{\Delta}y(s). \quad (13)$$

The transformed model parameters  $\tilde{a}_t$ ,  $\tilde{b}_t$ , and  $\tilde{c}_t$  can be directly estimated from the reference slice  $y_0(s)$  and the observed slice  $y_t(s)$ . The details of parameter estimation will be discussed in Section “Estimation of Model Parameters”. The bias term  $\tilde{\Delta}y(s)$  can be estimated by:

$$\widehat{\Delta}y(s) = \sum_{t=1}^N y_0(s) - y'_t(s), \quad (14)$$

where  $N$  is the number of observation. An estimate for the transformed noise terms,  $\tilde{\epsilon}_t(s)$ , can be obtained as:

$$\hat{\epsilon}_t(s) = y_0(s) - y'_t(s) - \widehat{\Delta}y(s). \quad (15)$$

Although the function  $\bar{\Psi}(s)$  cannot be observed or extracted from the observations, the transformation presented in (12) maps all the wavelet slices to the same reference in term of signal energy and bandwidth. The transformed error terms, as well as the estimated model parameters, can be used to test whether the slices are indeed drawn from the undamaged distribution. The case where not all slices are drawn from the undamaged distribution implies that damage has occurred in the structure.

The measurement noise of  $a(u)$  may affect the accuracy of the damage detection. A common way to model the measurement noise is the additive Gaussian noise. Hence, in the frequency domain, the measurement noise uniformly affects all frequency bands. When the signal to noise ratio (SNR) is high, the measurement noise has limited impact on the damage detection. In Section 4.2, we use the wired sensor signals to conduct damage detection. Usually, the wired sensors have low noise levels and high SNR.

#### 4.1 Estimation of Model Parameters

As discussed in [33, 34], the model parameters can be estimated by using the maximum likelihood estimation method. A key assumption is that the transformed error term,  $\tilde{\epsilon}_t(s)$ , follows an independently, with respect to the time, and identically distributed Gaussian Processes. With this assumption, the log-likelihood function of model parameters is (16), where  $M$  denotes the dimension of  $\tilde{\epsilon}_t$ , which is also the number of scales used to compute the wavelet transform, and  $\Sigma$  is the covariance matrix of the residual. In (16),  $y_t$  and  $y_0$  are  $M$ -dimensional vectors and  $\tilde{a}_t$ ,  $\tilde{b}_t$ , and  $\tilde{c}_t$  are scales. To solve (18), we present the following iterative algorithm to estimate the model parameters and residuals numerically:

1. Initialize  $\widehat{\Delta y}$  and  $\Sigma_{\tilde{\epsilon}}$  to an uninformed prior. In the present analysis,  $\widehat{\Delta y} = 0$  and  $\Sigma = I$ , where  $I$  is the  $M \times M$  identity matrix.
2. For  $t = 1 \dots N$ , calculate the parameters  $\hat{a}_t$ ,  $\hat{b}_t$ ,  $\hat{c}_t$  using maximum likelihood estimation.
3. Calculate the transformed slices by (12).
4. Calculate the bias term by (14).
5. Calculate the error terms by (15).
6. Estimate the covariance matrix from the error terms.
7. Repeat Steps 2 through 6 until the bias term and covariance matrix converge.

This algorithm only needs to be applied to the reference signal where the structure is assumed to be undamaged. Once the parameters are estimated, the covariance matrix  $\Sigma$  and the bias term  $\widehat{\Delta y}$  will refer to the undamaged state and be unchanged. When a new observation  $y_t$  is available, we only need to estimate the model parameters.

$$\begin{aligned} [\hat{a}, \hat{b}, \hat{c}, \hat{\Delta y}, \hat{\Sigma}] &= \underset{\tilde{a}, \tilde{b}, \tilde{c}, \Delta y, \Sigma}{\text{argmax}} \sum_{t=1}^N l(y_0 | y_t; \tilde{a}_t, \tilde{b}_t, \tilde{c}_t, \Delta y, \Sigma) \\ &= \underset{\tilde{a}, \tilde{b}, \tilde{c}, \Delta y, \Sigma}{\text{argmax}} \sum_{t=1}^N \log \left( (2\pi)^{-\frac{M}{2}} |\Sigma|^{-\frac{1}{2}} \exp -\frac{1}{2} \hat{\epsilon}_t^T \Sigma^{-1} \hat{\epsilon}_t \right) \end{aligned} \quad (16)$$

$$= \underset{\tilde{a}, \tilde{b}, \tilde{c}, \Delta y, \Sigma}{\text{argmax}} \sum_{t=1}^N -\frac{M}{2} \log(2\pi) - \frac{1}{2} \log(|\Sigma|) - \frac{1}{2} \hat{\epsilon}_t^T \Sigma^{-1} \hat{\epsilon}_t \quad (17)$$

$$= \underset{\tilde{a}, \tilde{b}, \tilde{c}, \Delta y, \Sigma}{\text{argmin}} \sum_{t=1}^N \log(|\Sigma|) + (y_0 - \tilde{a}_t y_t (\tilde{b}_t s + \tilde{c}_t) - \Delta y)^T \Sigma^{-1} \\ \times (y_0 - \tilde{a}_t y_t (\tilde{b}_t s + \tilde{c}_t) - \Delta y) \quad (18)$$

In (18), we need to compute the inverse of the covariance matrix. For high-dimensional data, the direct computation of the inverse covariance matrix may produce numerically unstable results. High dimensional inverse covariance matrix estimation has been well studied in literature, such as [35, 36, 37, 38]. In the subsequent section, a Matern covariance function [39] will be used and the fitting will be performed using the Gaussian Processes for Machine Learning (GPML) toolbox [40].

#### 4.2 Experimental Results

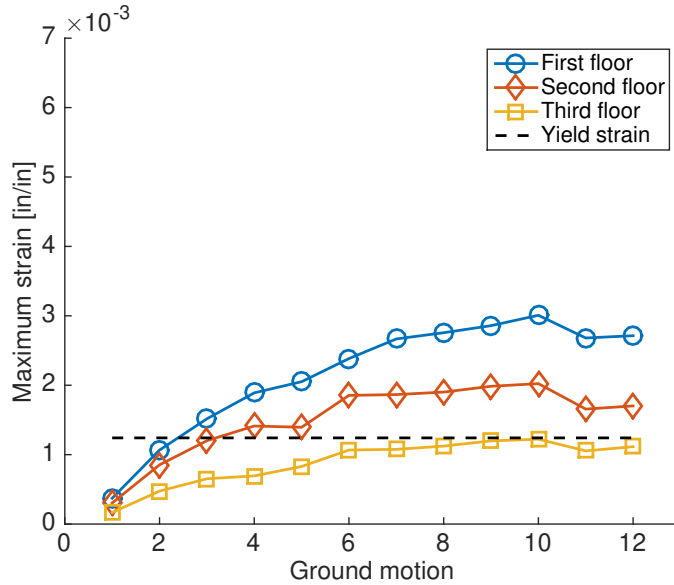


**Figure 12:** Maximum strain at each floor of Specimen 1, normalized by the steel's ultimate strain.

The CWT-based algorithm is applied to the acceleration measurements obtained from wired accelerometers. In order to evaluate the results of the damage detection algorithm, the presence or absence of damage is determined through the data obtained from strain gauges installed on the columns of both structures. Fig. 12 and Fig. 13 show the maximum strain at each floor for each ground motion of Specimen 1 and Specimen 2 respectively. The strains reported have been normalized by the ultimate strain ( $\epsilon_u$ ) of the steel used to highlight the fact that, while the structure did behave non-linearly, the overall level of damage sustained

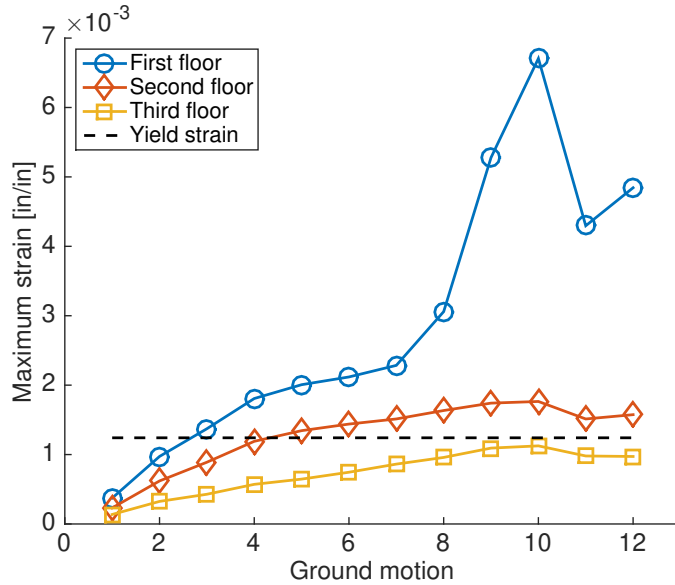


**Figure 13:** Maximum strain at each floor of Specimen 2, normalized by the steel's ultimate strain.

was very low. The dashed line is the threshold of damage. For both specimens, the first floors start to have damage in Run 3. For the third floors, we do not expect to see any damage. Compared with Run 10, the strains of Run 11 and Run 12 are reduced. This behavior is caused by the fact that we change the total masses of both structures.

The transformed residual terms  $\hat{\epsilon}_t(s)$  for each floor and selected runs are plotted in Fig. 14 for Specimen 1 and in Fig. 15 for Specimen 2. At the first floor of Specimen 1, during Run 6, the residual terms exhibit an extended interval of outliers, which can be observed as blue regions between scales 10 and 20. Similarly, at the second and third floors, we can see the blue outliers during Run 6. For the weakened specimen, the outliers can be observed on the first floor. With the damage progresses, the area of blue grows up. Furthermore, for both specimens, the residuals in Run 11 appear significantly different to the baseline. This is due to the fact that there was an additional mass on the roof of both structures for Run 11 and 12. Clearly, a change in loading conditions is detected for these two runs.

Compared with Specimen 1, Specimen 2 exhibits more consistent behavior in the undamaged state, e.g. Run 1 and Run 2, and more outlying intervals when damage occurs, e.g. Run 6, Run 9 and Run 11. The residuals in the first floor for both specimens appear more sensitive to damage. This observation is consistent with the plots in Fig. 12 and Fig. 13, where the strains of the first floors have the significant change after damage occurs. However, the first floors do not show consistent behavior while the structures remain undamaged. Conversely, the top two floors are more consistent in the undamaged state and, while they do exhibit intervals that can be interpreted as damage, appear less sensitive to damage compared to the first floor.

In order to evaluate the distributions of the residual terms, a Kernel Density Estimate (KDE) for the transformed residual terms at each scale is calculated and the results are plotted as heat maps in Fig. 16 for Specimen 1 and Fig. 17 for Specimen 2. In these two

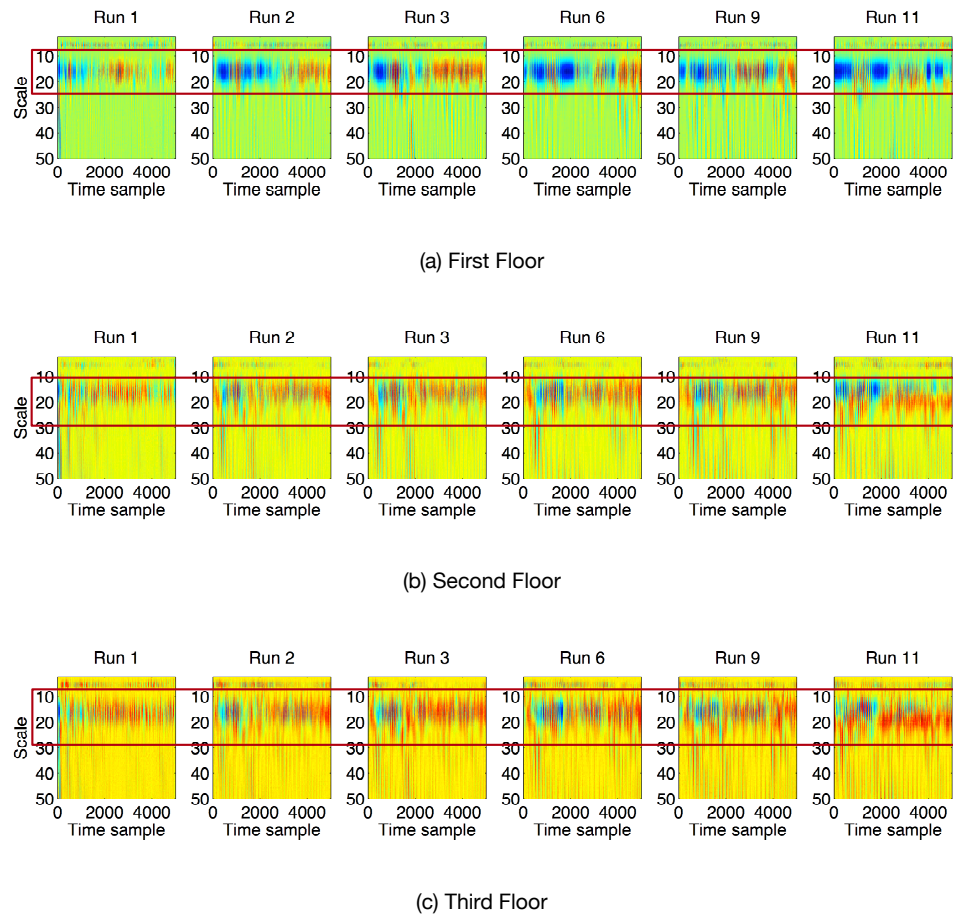


**Figure 14:** Residual terms for Specimen 1 (full strength specimen) and six different experimental runs. The red rectangular highlights the bands with changes before and after damage.

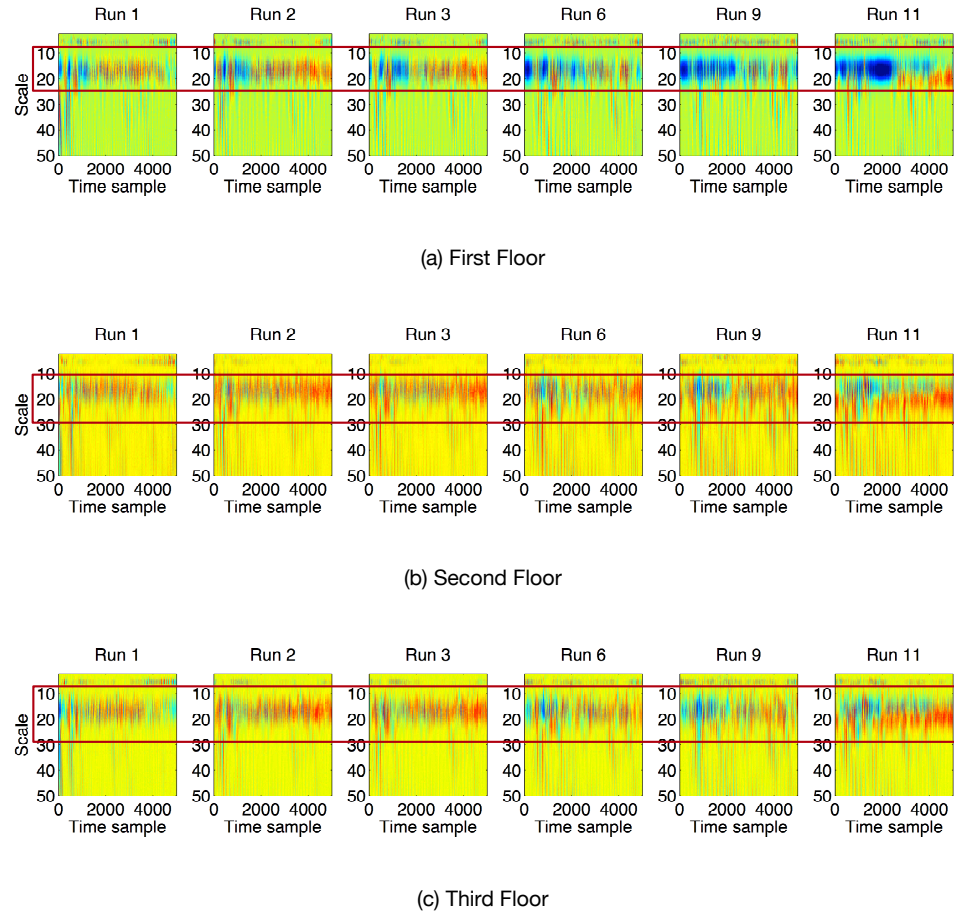


**Figure 15:** Residual terms for the weakened specimen (Specimen 2) and six different experimental runs. The red rectangular highlights the bands with changes before and after damage.

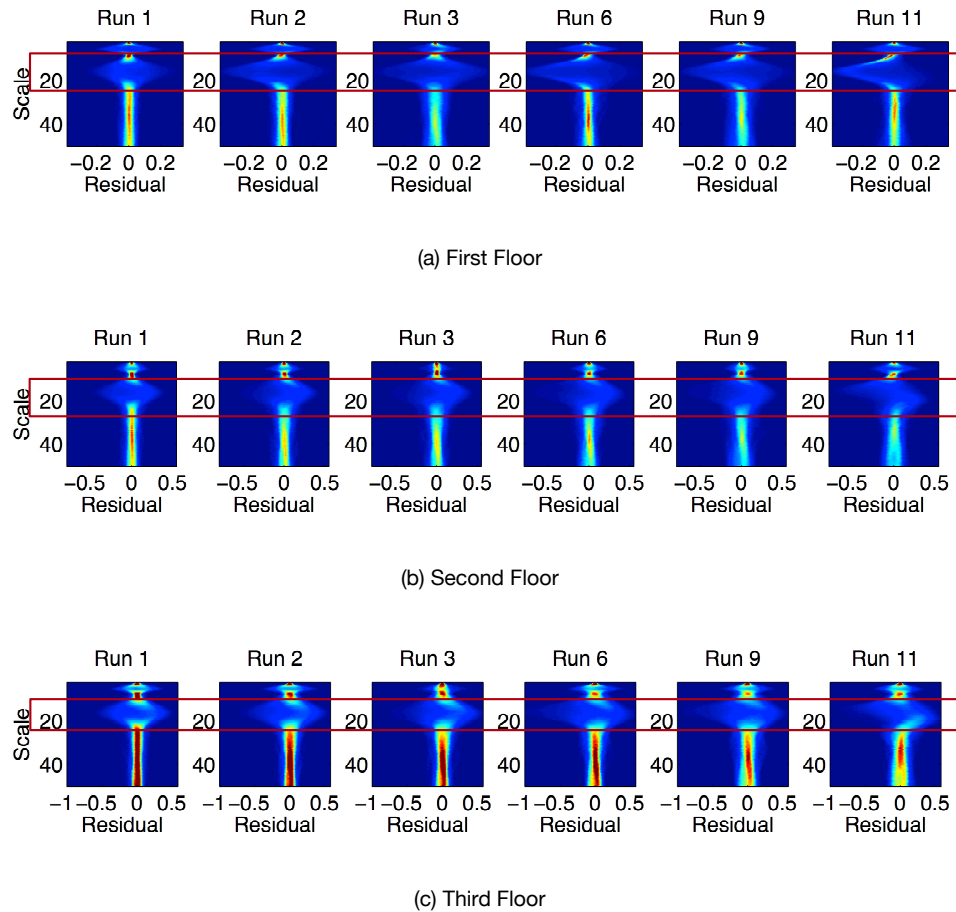


**Figure 16:** KDE of the residual terms for Specimen 1 (full strength specimen) and six different experimental runs. The red rectangular highlights the bands with changes before and after damage.

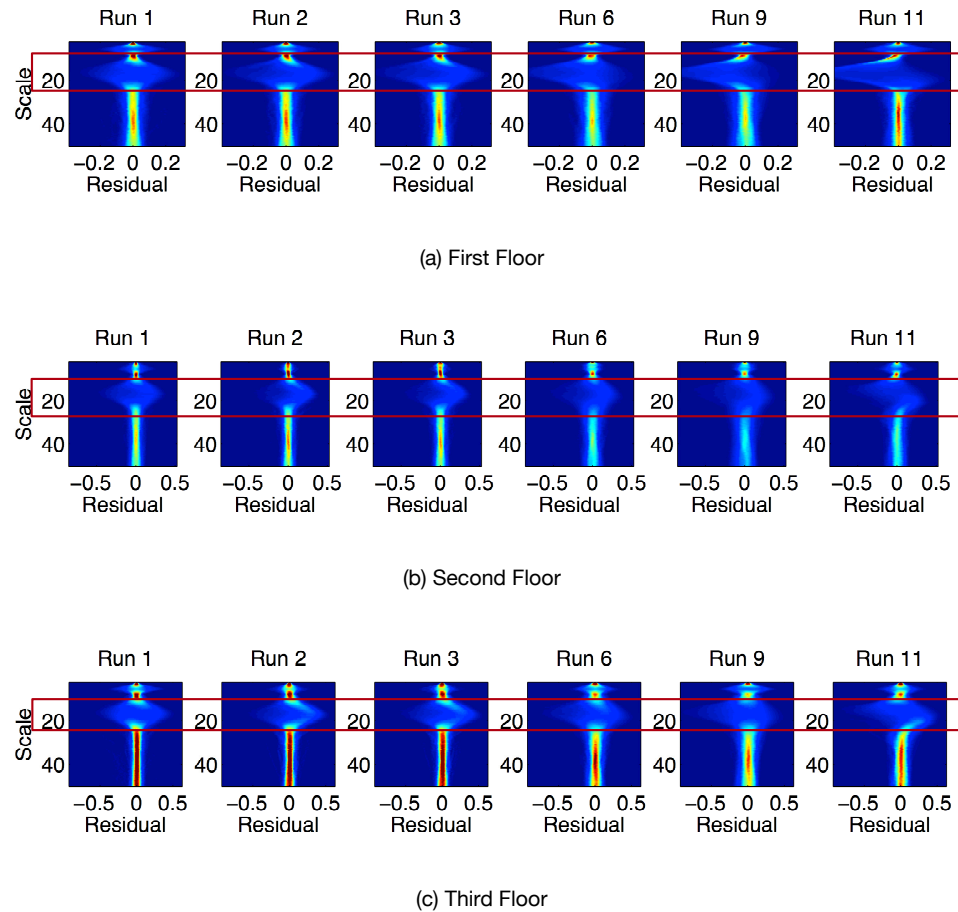


**Figure 17:** KDE of the residual terms for Specimen 2 (weakened specimen) and six different experimental runs. The red rectangular highlights the bands with changes before and after damage.

figures, each row of pixels corresponds to the KDE for the residual terms at the scale indicated on the y-axis.

As we have discussed previously, the residual terms should follow the same distribution while the structure remains undamaged and that distribution changes with the progression of damage. It can be observed that the residual distributions are more in agreement with the true damage state since the distributions in the undamaged state (Runs 1 and 2) are very similar to one another while the images change when damage occurs. In some cases, it appears as though Run 3 (the first occurrence of damage) is closer to the undamaged state but there are significant changes for Runs 6 and 9, where the extent of damage is greater. Finally, it is interesting to point out that the biggest changes in the distribution images occur in Run 11, indicating that the residual distributions are capable of identifying a change in the dynamic properties of the structure such as the additional mass in Run 11.

Fig. 18 and Fig. 19 show KDEs of the stretch parameters for all experimental runs. From these figures, we can observe that the distributions are much clearer than the residuals in indicating the presence or absence of damage. For the undamaged runs, e.g. Run 1 and Run 2, the parameter distributions are very similar. When a damage is presented, such as Run 3-10, we can observe a significant change and a progressive deviation from the initial distribution as the damage extent increases. As mentioned previously, in Run 11 and Run 12, an additional 500kg mass block was placed on the roof of each specimen. From these two figures, a clear jump can be observed. This observation indicates that the parameter distributions are sensitive to the loading conditions as well. Fig. 20 and Fig. 21 show KDEs of the shift parameters for all experiment runs. They have the similar behaviors as the KDEs of the stretch parameters. Therefore, the change in distribution is more easily observed in the distributions of the stretch and shift parameters of the model.

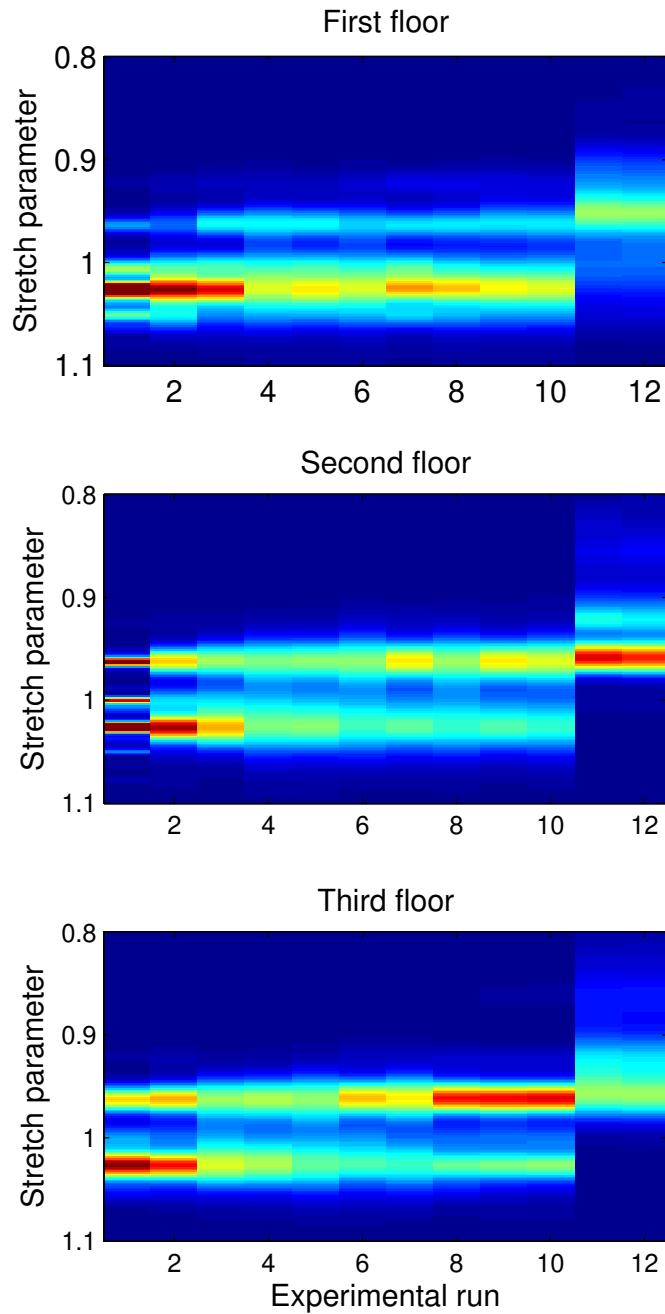


**Figure 18:** KDE of the stretch parameter of Specimen 1 for each experimental run.

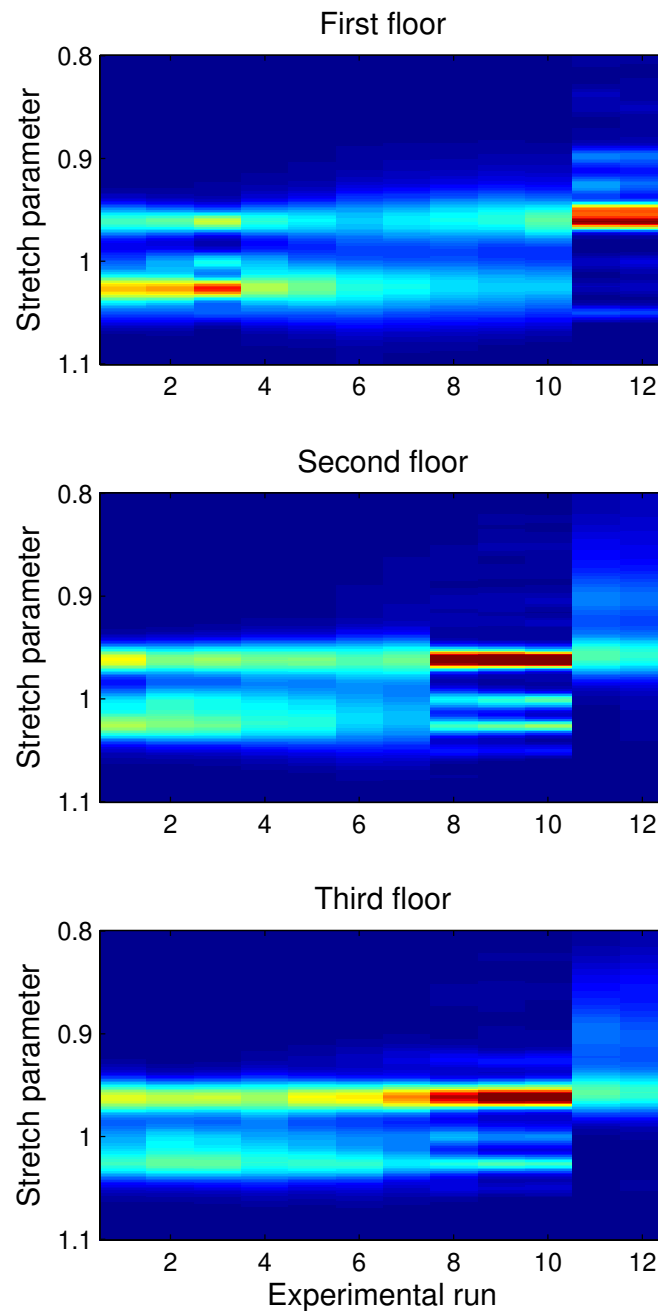


**Figure 19:** KDE of the stretch parameter of Specimen 2 for each experimental run.

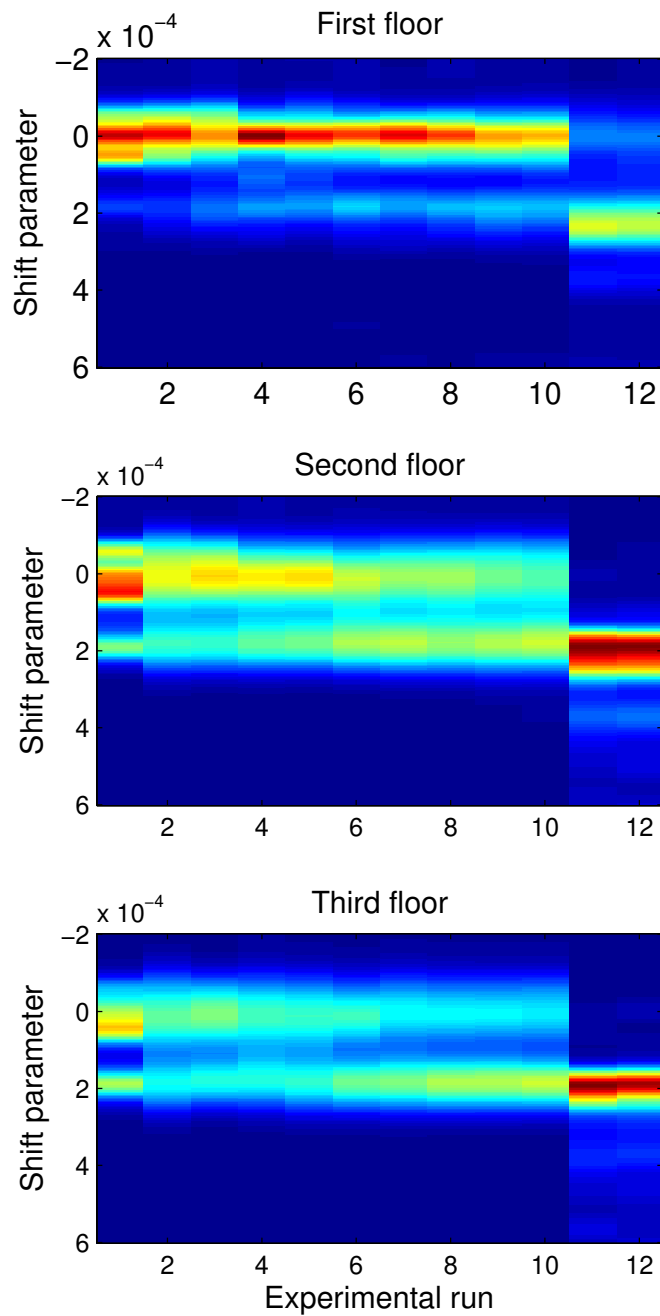


**Figure 20:** KDE of the shift parameter of Specimen 1 for each experimental run.

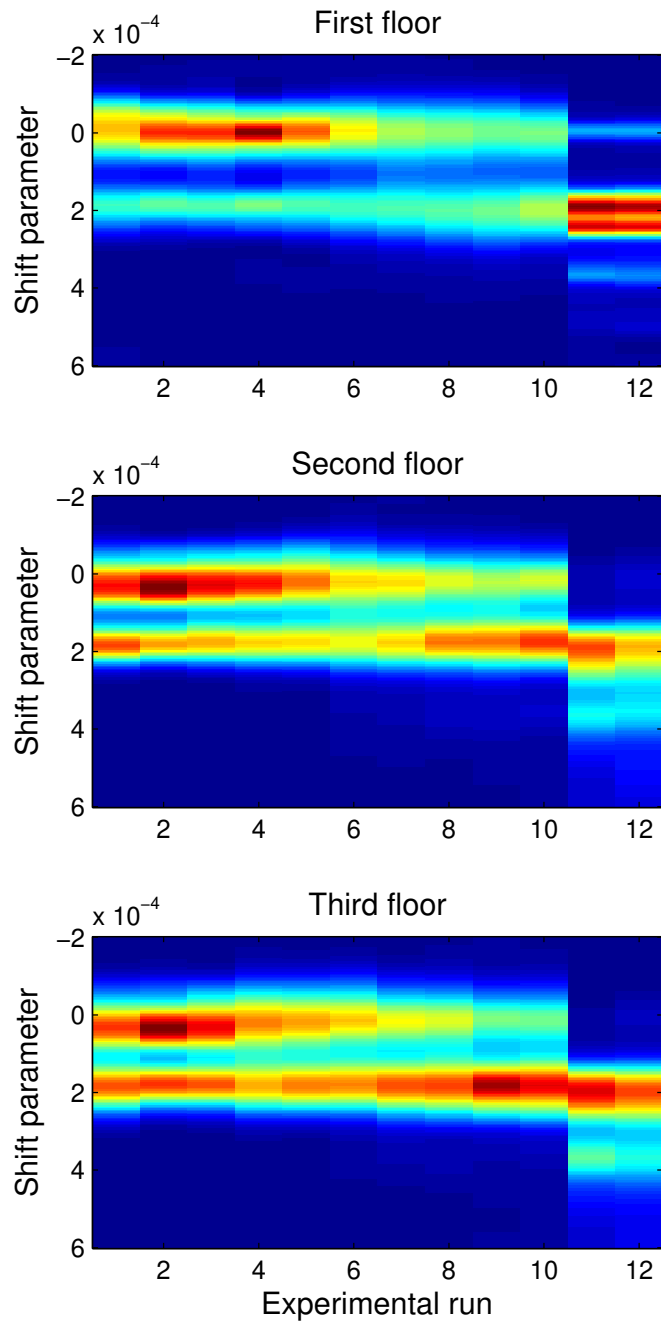


**Figure 21:** KDE of the shift parameter of Specimen 2 for each experimental run.

## 5 Conclusions and Future Works

This paper presents the analysis of data obtained from a recent shake table test on two steel frame structures with multiple types of sensors installed. We analyzed and discussed the performance and the accuracy of a new wireless monitoring system, SnowFort. It is demonstrated that SnowFort is a reliable and power efficient system for structural health monitoring. From the data collected, it is shown that the wireless accelerometers can achieve the same accuracy as the wired system. The Rotation Algorithm is designed for quickly measuring the permanent displacement before and after earthquakes. We have demonstrated that the proposed algorithm can be rapidly implemented for real-world applications by installing the wireless accelerometers on damaged structure. The experiment data are used to evaluate the residual displacement based on the Rotation Algorithm. Excellent agreement is found between the estimated residual displacements using the wireless accelerometer measurements and those obtained from direct measurements using LVDTs. The gaps between the estimated and measured residual displacements are the order of 1mm or less. Therefore, it suggests that we can replace LVDTs with wireless accelerometers for the measurements of residual displacement in the future experiments. The wavelet-based damage detection algorithm models the wavelet coefficients as the Gaussian process and provides a more reliable and accurate method to diagnose the structural damage status, compared with other wavelet-based methods. While the wavelet-based damage detection algorithm was initially demonstrated with numerically simulated data, applications of the algorithm to the data obtained from this experiment further confirm the observation that the algorithm is capable of detecting damage on structures subjected to severe vibrations. The results presented in this paper provide further validation of two main algorithms that were previously developed. Such confirmation is essential prior to field deployment of any structural health monitoring system.

The proposed sensor network and damage detection methods can be further validated in other types of applications. We have validated the SnowFort system in an indoor experiment setup. In many applications, such as bridge health monitoring, the sensors are usually installed in outdoor environment and may be exposed to high temperature, high pressure, and other extreme environment. Therefore, it requires more tests on the reliability and adaptability of the SnowFort system. The Rotation Algorithm has shown accurate results on estimating the residual displacement. However, we still need to explore how the sensor location and sensor network density impact the displacement estimation. Also, for some large-scale structures, the displacement may be very small. How to detect small displacement remains a research question. In addition, many research projects have focused on estimating the dynamic displacement and rotation during the earthquake. Therefore, another research direction is extending the proposed rotation algorithm to estimate the dynamic displacement. In the experiment of the wavelet-based damage detection method, we used the wired sensor data to detect structural damage. As we discussed in Section 2.2, wireless sensor systems have many advantages over wired systems. Therefore, we need to validate the wavelet-based algorithm using the wireless sensor data. Also, the current method requires estimating the model parameters with high computational complexity, as shown in Equation (18). Therefore, simplifying the computational complexity will make the method more suitable for real-time applications. Furthermore, the current damage detection is conducted via visual inspection. Recent approaches that using statistical pattern recognition, such as [34, 41, 42], offer new opportunities to utilize the statistical properties

to achieve better detection performance, such as shorter detection time and lower probability of false alarm.

## Dedication

This paper is dedicated to our dear friends Professor Lucia Faravelli and Professor Fabio Casciati on the occasion of their retirement from a long and highly successful career. It has been a true privilege for us to have known and worked with both of them for more than thirty five years. Our interactions have been fruitful, enlightening and productive. I hope to continue to work with them in their retirement for many years to come.

## References

- [1] EA Johnson, HF Lam, LS Katafygiotis, and JL Beck. Phase i iasc-asce structural health monitoring benchmark problem using simulated data. *Journal of Engineering Mechanics*, 130(1):3–15, 2004.
- [2] Charles R Farrar, Scott W Doebling, and David A Nix. Vibration-based structural damage identification. *Philosophical Transactions of the Royal Society of London A: Mathematical, Physical and Engineering Sciences*, 359(1778):131–149, 2001.
- [3] C. R. Farrar and K. Worden. An introduction to Structural Health Monitoring. *The Royal Society – Philosophical Transactions: Mathematical, Physical and Engineering Sciences*, 365:303–315, 2007.
- [4] Charles R Farrar and Keith Worden. *Structural health monitoring: a machine learning perspective*. John Wiley & Sons, 2012.
- [5] Edward Sazonov, Kerop Janoyan, and Ratan Jha. Wireless intelligent sensor network for autonomous structural health monitoring. In *Smart Structures and Materials*, pages 305–314. International Society for Optics and Photonics, 2004.
- [6] Sukun Kim, S. Pakzad, D. Culler, J. Demmel, G. Fenves, S. Glaser, and M. Turon. Health monitoring of civil infrastructures using wireless sensor networks. In *Information Processing in Sensor Networks, 2007. IPSN 2007. 6th International Symposium on*, pages 254–263, April 2007.
- [7] Shamim N Pakzad, Gregory L Fenves, Sukun Kim, and David E Culler. Design and implementation of scalable wireless sensor network for structural monitoring. *Journal of Infrastructure Systems*, 14(1):89–101, 2008.
- [8] Tyler Harms, Sahra Sedigh, and Filippo Bastianini. Structural health monitoring of bridges using wireless sensor networks. *Instrumentation & Measurement Magazine, IEEE*, 13(6):14–18, 2010.
- [9] Hoon Sohn, Charles R Farrar, Norman F Hunter, and Keith Worden. Structural health monitoring using statistical pattern recognition techniques. *Journal of dynamic systems, measurement, and control*, 123(4):706–711, 2001.

- [10] Hoon Sohn and Charles R Farrar. Damage diagnosis using time series analysis of vibration signals. *Smart materials and structures*, 10(3):446, 2001.
- [11] Michael L Fugate, Hoon Sohn, and Charles R Farrar. Vibration-based damage detection using statistical process control. *Mechanical Systems and Signal Processing*, 15(4):707–721, 2001.
- [12] YJ Yan, L Cheng, ZY Wu, and LH Yam. Development in vibration-based structural damage detection technique. *Mechanical Systems and Signal Processing*, 21(5):2198–2211, 2007.
- [13] M Chandrashekhar and Ranjan Ganguli. Uncertainty handling in structural damage detection using fuzzy logic and probabilistic simulation. *Mechanical Systems and Signal Processing*, 23(2):384–404, 2009.
- [14] F Magalhães, A Cunha, and E Caetano. Vibration based structural health monitoring of an arch bridge: from automated oma to damage detection. *Mechanical Systems and Signal Processing*, 28:212–228, 2012.
- [15] Wei Fan and Pizhong Qiao. Vibration-based damage identification methods: a review and comparative study. *Structural Health Monitoring*, 10(1):83–111, 2011.
- [16] Yizheng Liao, M. Mollineaux, R. Hsu, R. Bartlett, A. Singla, A. Raja, R. Bajwa, and R. Rajagopal. Snowfort: An open source wireless sensor network for data analytics in infrastructure and environmental monitoring. *Sensors Journal, IEEE*, 14(12):4253–4263, Dec 2014.
- [17] Konstantinos Balafas and Anne S Kiremidjian. Extension of the rotation algorithm for earthquake damage estimation of complex structures. In *SPIE Smart Structures and Materials+ Nondestructive Evaluation and Health Monitoring*, pages 86920S–86920S. International Society for Optics and Photonics, 2013.
- [18] Konstantinos Balafas, Ram Rajagopal, and Anne S Kiremidjian. The continuous wavelet transform as a stochastic process for damage detection. In *12th International Conference on Applications of Statistics and Probability in Civil Engineering*, 2015.
- [19] Joseph Polastre, Robert Szewczyk, and David Culler. Telos: enabling ultra-low power wireless research. In *Information Processing in Sensor Networks, 2005. IPSN 2005. Fourth International Symposium on*, pages 364–369. IEEE, 2005.
- [20] Moteiv. Tmote sky datasheet. Data sheet, 2006.
- [21] InvenSense. Mpu-6000 and mpu-6050 product specification revision 3.4. Data sheet, 2013.
- [22] SnowFort. Snowfort website. Website, 2013. Accessed: 2015-10-29.
- [23] Eben Upton and Gareth Halfacree. *Raspberry Pi user guide*. John Wiley & Sons, 2014.
- [24] Jeongyeup Paek, Krishna Chintalapudi, John Caffrey, Ramesh Govindan, and Sami Masri. A wireless sensor network for structural health monitoring: Performance and experience. *Center for Embedded Network Sensing*, 2005.

- [25] Maurizio Bocca, Lasse M Eriksson, Aamir Mahmood, Riku Jäntti, and Jyrki Kullaa. A synchronized wireless sensor network for experimental modal analysis in structural health monitoring. *Computer-Aided Civil and Infrastructure Engineering*, 26(7):483–499, 2011.
- [26] Allen Cheung and Anne S Kiremidjian. Development of a rotation algorithm for earthquake damage diagnosis. *Earthquake Spectra*, 30(4):1381–1401, 2014.
- [27] T Paulay and MJN Priestly. Principles of member design. *Seismic design of reinforced concrete and masonry buildings*, pages 95–157, 1992.
- [28] Vu Phan, M Saiid Saiidi, John Anderson, and Hamid Ghasemi. Near-fault ground motion effects on reinforced concrete bridge columns. *Journal of structural engineering*, 133(7):982–989, 2007.
- [29] Z Hou, M Noori, and R St Amand. Wavelet-based approach for structural damage detection. *Journal of Engineering mechanics*, 126(7):677–683, 2000.
- [30] MAGDALENA Rucka and KRZYSZTOF Wilde. Application of continuous wavelet transform in vibration based damage detection method for beams and plates. *Journal of Sound and Vibration*, 297(3):536–550, 2006.
- [31] Hansang Kim and Hani Melhem. Damage detection of structures by wavelet analysis. *Engineering Structures*, 26(3):347–362, 2004.
- [32] Konstantinos Balafas. *Development and evaluation of acceleration-based earthquake damage detection and classification algorithms*. PhD thesis, Stanford University, 2015.
- [33] Konstantinos Balafas, Ram Rajagopal, and Anne S. Kiremidjian. The wavelet transform as a gaussian process for damage detection: Model formulation. *Journal of Engineering Mechanics (submitted for publication)*, 2015.
- [34] Yizheng Liao, Konstantinos Balafas, Ram Rajagopal, and Anne S Kiremidjian. Sequential damage detection based on the continuous wavelet transform. In *SPIE Smart Structures and Materials+ Nondestructive Evaluation and Health Monitoring*, pages 94350S–94350S. International Society for Optics and Photonics, 2015.
- [35] T. W. Anderson. Asymptotically efficient estimation of covariance matrices with linear structure. *The Annals of Statistics*, 1(1):135–141, January 1973.
- [36] Donald W. K. Andrews. Heteroskedasticity and autocorrelation consistent covariance matrix estimation. *Econometrica*, 59(3):817–858, May 1991.
- [37] Yilun Chen, A. Wiesel, Y. C. Eldar, and AO. Hero. Shrinkage algorithms for MMSE covariance estimation. *IEEE Transactions on Signal Processing*, 58(10):5016–5029, October 2010.
- [38] Ming Yuan. High dimensional inverse covariance matrix estimation via linear programming. *The Journal of Machine Learning Research*, 11:2261–2286, 2010.
- [39] Budiman Minasny and Alex B McBratney. The matérn function as a general model for soil variograms. *Geoderma*, 128(3):192–207, 2005.

- [40] Carl Edward Rasmussen and Christopher K. I. Williams. *Gaussian Processes for Machine Learning*. The MIT Press, 2006.
- [41] Hae Young Noh, K. Krishnan Nair, Dimitrios Lignos, and Anne S. Kiremidjian. Use of wavelet-based damage-sensitive features for structural damage diagnosis using strong motion data. *Journal of Structural Engineering*, 137(10):1215–1228, October 2011.
- [42] Yizheng Liao, Anne S Kiremidjian, Ram Rajagopal, and Chin-Hsuing Loh. Structural damage detection and localization with unknown postdamage feature distribution using sequential change-point detection method. *Journal of Aerospace Engineering*, 32(2):04018149, 2018.